The Astrophysical Journal, 954:1 (8pp), 2023 September 1 https://doi.org/10.3847/1538-4357/ace699

Hadronic versus Leptonic Origin of Gamma-Ray Emission from Supernova Remnants

Nicholas J. Corso[1,2], Rebecca Diesing[1], and Damiano Caprioli[1,3]
[1] Department of Astronomy and Astrophysics, The University of Chicago, 5640 South Ellis Avenue, Chicago, IL 60637, USA; njc86@cornell.edu
[2] Department of Astronomy, Cornell University, 404 Space Sciences Building, Ithaca, NY 14853, USA
[3] Enrico Fermi Institute, The University of Chicago, Chicago, IL 60637, USA
Received 2023 January 23; revised 2023 June 15; accepted 2023 July 10; published 2023 August 18

Abstract

GeV and TeV emission from the forward shocks of supernova remnants (SNRs) indicates that they are capable particle accelerators, making them promising sources of Galactic cosmic rays (CRs). However, it remains uncertain whether this γ-ray emission arises primarily from the decay of neutral pions produced by very-high-energy hadrons, or from inverse-Compton and/or bremsstrahlung emission from relativistic leptons. By applying a semi-analytic approach to non-linear diffusive shock acceleration, and calculating the particle and photon spectra produced in different environments, we parameterize the relative strength of hadronic and leptonic emission. We show that even if CR acceleration is likely to occur in all SNRs, the observed photon spectra may primarily reflect the environment surrounding the SNR: the emission is expected to look hadronic unless the ambient density is particularly low (with proton number density $\lesssim 0.1\ \mathrm{cm}^{-3}$) or the photon background is enhanced with respect to average Galactic values (with radiation energy density $u_{\mathrm{rad}} \gtrsim 10\ \mathrm{eV\ cm}^{-3}$). We introduce a hadronicity parameter to characterize how hadronic or leptonic we expect a source to look based on its environment, which can be used to guide the interpretation of current γ-ray observations and the detection of high-energy neutrinos from SNRs.

Unified Astronomy Thesaurus concepts: Cosmic ray astronomy (324); Galactic cosmic rays (567); Cosmic ray sources (328); High-energy cosmic radiation (731); Supernova remnants (1667); Shocks (2086)

1. Introduction

The forward shocks of supernova remnants (SNRs) are promising candidates for the primary sources of Galactic cosmic rays (CRs) because they provide sufficient energetics and an efficient acceleration mechanism, which is diffusive shock acceleration (DSA; O'C. Drury et al. 1994; Hillas 2005; Berezhko & Völk 2007; Caprioli et al. 2010a; Ptuskin et al. 2010). However, direct evidence of efficient hadron acceleration by SNRs, particularly up to the so-called "CR knee" at energies $\gtrsim 10^{15}$ eV, remains limited (Blasi 2019).

The best observational evidence for hadron acceleration is >100 MeV γ-ray emission from the decay of neutral pions (π_0) produced by interactions between CR ions and the ambient medium (O'C. Drury et al. 1994), as well as high-energy neutrinos from the decay of charged pions in the same reaction. However, when leptons—primarily electrons—are accelerated, they too can produce strong γ-ray signatures via inverse-Compton (IC) and relativistic bremsstrahlung radiation (Aharonian et al. 2006). Ideally, observational signatures would identify which of the two scenarios dominates, but in many cases the results are ambiguous.

One example of this ambiguity is RX J1713.7-3946, which was identified as a source of high-energy γ-ray emission when it was detected in the TeV band by the HESS collaboration (Aharonian et al. 2006). As demonstrated in Morlino et al. (2009), both hadronic and leptonic scenarios can explain observed HESS data. However, later data from Fermi-LAT favored leptonic models, apparently indicating that RX J1713.7-3946 and Vela Jr. are not efficient hadron accelerators (Ellison et al. 2010; Zirakashvili & Aharonian 2010; Abdo et al. 2011; Lee et al. 2013). Meanwhile, Morlino & Caprioli (2012) later identified Tycho's SNR as a strong candidate for hadronic γ-rays based on VERITAS and Fermi-LAT data. In addition, the detection of the characteristic "pion bump" in IC443 and W44 confirmed the hadronic nature of the γ-ray emission from these SNRs interacting with molecular clouds (Ackermann et al. 2013). The recent measurement of the nova RS Ophiuchi, which was characterized as solidly hadronic, serves as an example of this ongoing exploration (Acciari et al. 2022; Aharonian et al. 2022; Diesing et al. 2023). These findings raise questions about whether hadronic emission from SNRs is common enough for them to be the primary accelerators of Galactic CRs.

Ideally, to assess the hadronic/leptonic nature of a source, multi-wavelength measurements would be made for all γ-ray bright SNRs in consideration, but this is time-consuming and often inconclusive due to the limiting constraints on age and distance.

In recent years, kinetic simulations of non-relativistic shocks have shown that the acceleration of protons and heavier nuclei is mostly controlled by the local inclination of the shock (i.e., the angle between the shock normal and the local magnetic field), rather than by the shock strength, parameterized by its sonic and Alfvénic Mach numbers (Caprioli & Spitkovsky 2014a, 2014b, 2014c; Caprioli et al. 2017, 2018; Haggerty & Caprioli 2020). Conversely, the efficiency of electron acceleration in such shocks is not fully understood yet (for more on this subject, see the works by Guo et al. 2014; Park et al. 2015; Xu et al. 2020; Shalaby et al. 2022).

Since most SNRs are likely to have a variety of shock inclinations (Pais & Pfrommer 2020; Winner et al. 2020), we do not expect the acceleration efficiency to vary greatly in all of the SNRs that exhibit strong shocks. Therefore, we propose that environmental factors are essential determiners of the dominant emission mechanism. That is, we consider how the

age and the characteristics of the medium in which SNRs expand (i.e., density profile and normalization, and energy density of background radiation) impact their γ-ray production, and thus its inferred hadronic/leptonic nature.

The suggestion that environmental factors play dominant roles in the emission signatures from SNRs has previously been explored (e.g., Ellison et al. 2007; Yuan et al. 2012), but this study expands upon these works by incorporating the state-of-the-art DSA theory, which is also validated by kinetic simulations. We apply a semi-analytic formalism for non-linear DSA to calculate the particle and photon spectra at various stages in the evolution of simulated SNRs. Particle spectra are determined self-consistently from the instantaneous shock properties, including the generation of magnetic turbulence via CR-driven instabilities, which affects the particle spectral slope (Caprioli et al. 2020) and the cooling of electrons (Diesing & Caprioli 2019). Using these spectra, we parameterize the relative strength of hadronic and leptonic emission to assess when the former dominates over the latter.

Our analysis, which leverages the relative normalization and spectral slopes of different kinds of γ-ray emission, provides information about when and where SNRs are most likely to exhibit a hadronic signature. We construct effective "lookup tables" that may guide the interpretation of the spectra currently available and of those that will be provided by the incoming generation of γ-ray and neutrino telescopes, such as LHAASO, CTA, and Ice Cube, KM3NET, TRIDENT, and so on.

This paper is organized as follows: in Section 2, we discuss the theoretical background of our computational model, along with the analytical tools which we use to present our results; and in Sections 3 and 4, we present and analyze our results, with the goal of providing a tool for quick estimation of a source's capacity to produce hadronic emission.

2. Method

In general, the evolution of a SNR follows four principal stages (e.g., Ostriker & McKee 1988; Bisnovatyi-Kogan & Silich 1995; Diesing & Caprioli 2018): in the ejecta-dominated stage, the ejected mass is much greater than the swept-up mass and the SNR expands effectively unimpeded; in the Sedov stage, the swept-up mass exceeds the ejected mass and the SNR expands adiabatically; in the pressure-driven snowplow, the SNR begins to lose energy to radiative cooling but continues to expand because its internal pressure exceeds that of the ambient background; finally, in the momentum-driven snowplow, expansion is driven by the residual kinetic energy from the explosion. For this work, only the ejecta-dominated and Sedov stages are considered because most of the SNRs seem to fade away in the radiative stage (e.g., Case & Bhattacharya 1998; Bandiera & Petruk 2010).

Broadly speaking, we consider two types of environments surrounding our model SNRs. In the first, we assume a homogeneous interstellar medium (ISM) with a uniform matter density. In the second, we model an environment that may exist around a core-collapse supernova, in which the medium is dominated by stellar winds driven by the supernova progenitor and exhibits an inverse square matter density profile ($n \propto R_{\rm sh}^{-2}$).

All simulated SNRs eject 1 $M_\odot$ of mass with $E = 10^{51}$ erg of kinetic energy. For the homogeneous profiles, we assume an ambient magnetic field strength of $B_0 = 3\,\mu$G, and we test ambient number density values spanning $n_0 \in [10^{-2}, 10^{1}]\,{\rm cm}^{-3}$. In the case of the wind profile, we represent the number density as $n(r) = n_0 (r/{\rm pc})^{-2}$. Our choice of n_0 is motivated by Weaver et al. (1977), who note that $\rho(r) \propto \dot{M}/(V_w r^2)$, where $\dot{M}$ is the mass loss rate of the progenitor and V_w is the speed of its stellar wind. Taking $\dot{M}_{-5,\odot}/V_{w,6}$ to vary around order unity, with $\dot{M} = \dot{M}_{-5,\odot} 10^{-5} M_\odot\ {\rm yr}^{-1}$ and $V_w = V_{w,6} 10^6\,{\rm km\,s}^{-1}$, we obtain and sample the following range of values: $n_0 \in [3.5 \times 10^{-2}, 7.5]\,{\rm cm}^{-3}$. Following Ptuskin & Zirakashvili (2005) and Caprioli (2011), and references therein, we adopt an ambient magnetic field strength profile that scales as the square root of the number density, normalized as $B_0 = B_*(r/{\rm pc})^{-1} \simeq (141\ \mu{\rm G}) n_0^{1/2} (r/{\rm pc})^{-1}$. Notice that with our current choice of n_0, our magnetic field normalization falls within the range $B_* \in [2.6 \times 10^1, 3.9 \times 10^2]\,\mu$G. Naively, these may appear to be rather large, especially when compared to the homogeneous profiles, but the adopted form is consistent with values observed in radio SNe (see Chevalier 1998). For the results of this paper, the downstream magnetic fields, which are calculated using the semi-analytic formalism for non-linear DSA that is described below, are more relevant. Indeed, we find these downstream fields to be both consistent with observed values and comparable in magnitude to the downstream fields of the homogeneous profiles.

We simulate CR acceleration using the semi-analytic formalism for non-linear DSA (NLDSA) that was described by Caprioli et al. (2009, 2010b), Caprioli (2012), and Diesing & Caprioli (2019), and references therein (Malkov 1997; Malkov et al. 2000; Blasi 2002, 2004; Amato & Blasi 2005, 2006). This model self-consistently solves the diffusion-advection equation for the transport of nonthermal particles in a quasi-parallel and non-relativistic shock, including the dynamical backreaction of accelerated particles and of CR-generated magnetic turbulence. Magnetic field amplification due to CR-driven streaming instabilities is taken into account as described in Diesing & Caprioli (2021). More precisely, fast shocks are dominated by the non-resonant (Bell) instability, while later in the Sedov stage the resonant instability becomes important (e.g., Bell 2004; Amato & Blasi 2009).

This formalism calculates the instantaneous proton spectrum at each timestep of the SNR's evolution. The minimum (injection) momentum occurs at $p_{\rm min} = \xi_{\rm inj} p_{\rm th}$, where $p_{\rm th}$ is the downstream thermal momentum, given by $p_{\rm th} = (4\gamma\sqrt{\gamma - 1}/(\gamma + 1)^2) m v_{\rm sh} \simeq 0.77 m v_{\rm sh}$ for $\gamma = 5/3$, where $v_{\rm sh}$ is the shock speed, and the value $\xi_{\rm inj} \simeq 3$–3.5 is chosen based on the simulations of Caprioli & Spitkovsky (2014a) and Caprioli et al. (2015). The maximum momentum is set by the finite size of the accelerator, namely the diffusion length at $p_{\rm max}$ becomes comparable to a given fraction of the shock radius, $\sim 0.1 R_{\rm sh}$. The diffusion coefficient is calculated assuming Bohm diffusion, i.e., with the mean free path for pitch-angle scattering equal to the particle gyroradius in the amplified magnetic field (Reville & Bell 2013; Caprioli & Spitkovsky 2014b). This scaling, which is identical to assuming that acceleration is time-limited (Lagage & Cesarsky 1983; Blasi et al. 2007), reads $p_{\rm max} \propto \sqrt{B_{\rm d} v_{\rm sh} R_{\rm sh}}$, with $B_{\rm d}$ the downstream magnetic field. The actual value of $p_{\rm min}$ controls the acceleration efficiency (e.g., Caprioli 2012), and we tune it to match kinetic simulations (Caprioli & Spitkovsky 2014a), while the value of $p_{\rm max}$ determines the highest-energy hadronic photon that can be produced and can

be inferred from the spectra presented here (see Diesing 2023 for more details).

As in Diesing & Caprioli (2019), we calculate the instantaneous electron spectra using the analytical approximation provided in Zirakashvili & Aharonian (2007),

$$f_e(p) = K_{ep} f_p(p)[1 + 0.523(p/p_{e,max})^{9/4}]^2 e^{-p^2/p_{e,max}^2}, \quad (1)$$

with K_{ep} the normalization of the electron spectrum relative to that of protons and $p_{e,max}$ the maximum electron momentum determined by equating the acceleration and synchrotron loss timescales (Zirakashvili & Aharonian 2007; Blasi 2010). For Bohm diffusion and typical shock compression of ∼4, this reads:

$$p_{e,max} \simeq 23.8 \text{ TeV} \left(\frac{v_{sh}}{3000 \text{ km s}^{-1}}\right)\left(\frac{B}{100\ \mu\text{G}}\right)^{1/2}. \quad (2)$$

Unless explicitly stated otherwise, we adopt the reference value of $K_{ep} = 1.6 \times 10^{-3}$, which corresponds to the value determined for Tycho's SNR in Morlino & Caprioli (2012), and discuss how the results change when varying this parameter over the range of $K_{ep} = 10^{-4}$–10^{-2}, which also encompasses the range of values inferred in other SNRs (Berezhko & Völk 2004, 2006; Berezhko et al. 2006; Lee et al. 2013). The instantaneous proton and electron spectra are then weighted to account for adiabatic and—in the case of electrons—synchrotron losses, before being summed to produce a cumulative spectrum (see Caprioli et al. 2010a; Diesing & Caprioli 2019, for more details).

To generate the spectrum of nonthermal radiation from a modeled SNR, we use the `Naima` Python package (Zabalza 2015), which, given arbitrary proton and electron momentum distributions, calculates the emission due to IC (Khangulyan et al. 2014), synchrotron (Aharonian et al. 2010), nonthermal bremsstrahlung assuming a fully ionized medium (Baring et al. 1999), and pion decay (Kafexhiu et al. 2014). In this work, we do not consider propagation in partly ionized media, which is considerably more complicated because of the potential role of ionization and charge exchange (see, e.g., Blasi et al. 2012; Morlino et al. 2013, and references therein). This prescription effectively maximizes nonthermal bremsstrahlung emission, but this does not affect our results since the process is typically subdominant.

We consider different background radiation fields, which are meant to mimic different astrophysical environments, on top of the ubiquitous cosmic microwave background (CMB) radiation, with a temperature of $T = 2.72$ K and an energy density $u_{rad} = 0.261$ eV cm^{-3}. An effective "maximal" radiation field would correspond to that of a HII environment, as described in Section 12.7 of Draine (2011), with an energy density of $u_{rad} \sim 4 \times 10^3$ eV cm^{-3}. To span the range of photon energy densities between these two extremes, we also consider an environment consisting of the CMB field and starlight peaking in the mid-infrared with a temperature of $T = 100$ K. We treat the energy density of this stellar radiation field as a free parameter. All spectra are calculated assuming a fixed source distance of 3 kpc, so that only their relative comparisons are important for the purposes of this study.

To interpret the dominant form of emission, we introduce a parameter H, which we name the hadronicity of the emitted radiation. This parameter is defined as:

$$H \equiv \frac{2}{\pi} \arctan\left[\log_{10}\left(\frac{L_{had}}{L_{lep}}\right)\right] \quad (3)$$

where $L_{had/lep}$ is the hadronic/leptonic luminosity integrated over a given energy band. While H can be retained as a function of energy, we focus on the GeV band, which is defined as 100 MeV–100 GeV, and the TeV band, which is defined as 100GeV–1 PeV. These bands broadly reflect the regimes of energy spanned by GeV and TeV observatories (i.e., Fermi and Cherenkov telescopes). Using this definition, a value of $0.75 < H \leqslant 1.$ is considered extremely hadronic, while $0. < H \leqslant 0.5$ corresponds to mildly hadronic. Conversely, similar absolute values of H but with negative sign would correspond to extremely and mildly leptonic cases. The hadronicity parameter H may be interpreted as the likelihood that the γ-ray emission of SNR with given characteristics (age, density, magnetic field, photon background) is of hadronic origin.

For practical purposes, H is meant to provide an informed guess about the hadronic/leptonic nature of the GeV or TeV emission from a given SNR without the need to perform a detailed time-dependent and multi-zone calculation of particle acceleration, and its ensuing multi-wavelength emission.

3. Results

The ion and electron spectra produced by a sample of SNRs expanding in different density profiles are shown in Figure 1. These spectra are the cumulative post-shock distributions calculated when the SNR transitions from the ejecta-dominated to the Sedov stage. This time, denoted T_{ST}, is evaluated to be the moment that the accumulated mass from the surrounding medium exceeds the originally ejected mass. Across the parameter space for both profiles, the particle spectra do not change dramatically, but it should be noted that p_{max} and $p_{e,max}$ vary slowly, resulting in changes in the high-energy cutoffs.

It is worth stressing that these spectra are steeper than the standard DSA prediction, $dN/dE \propto E^{-2}$, due to the shock modification induced by nonthermal particles and by the amplified magnetic they generate. In particular, we include the effects of the postcursor, i.e., the region immediately downstream of the shock where there is net drift of magnetic fluctuations and CRs with respect to the thermal plasma. These effects, which were seen for the first time in kinetic simulations (Caprioli et al. 2020; Haggerty & Caprioli 2020), lead to an enhanced shock compression and a steepening of the CR spectrum, both in excellent agreement with observations—see Diesing & Caprioli 2021 for a discussion on SNR spectra and Giuffrida et al. (2022) for the specific case of SN1006. This steepening of the particle spectra is most relevant to the results of our study because this will impact the behavior of the resulting photon spectra. In addition, electron spectra are cooled by IC and synchrotron losses, as pointed out by Diesing & Caprioli (2019) and discussed by Cristofari et al. (2021), Morlino & Celli (2021). Since the maximum electron energy is controlled by synchrotron losses, it is strongly dependent on the amplified magnetic field, which also correlates with the local density.

In Figure 2, we present a wide sample of modeled γ-ray spectra from SNRs in different environments, spanning the full

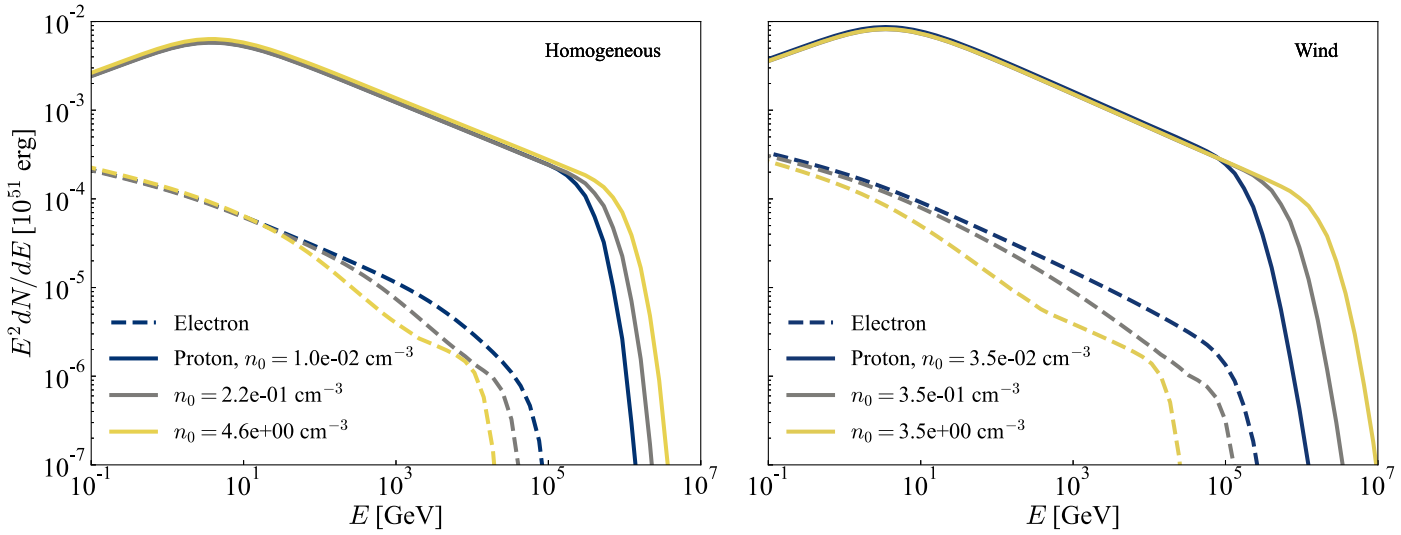

Figure 1. Cumulative proton spectra (solid lines) and electron spectra (dashed lines) at the transition between the ejecta-dominated and Sedov–Taylor stages of a modeled SNR in a sample of environments. Line colors denote the density normalization used in each model. In the left-hand panel, the ambient medium is taken to be homogeneous; in the right-hand panel, it follows a wind profile. The electron/proton normalization is fixed to $K_{ep} = 1.6 \times 10^{-3}$, as discussed in the text.

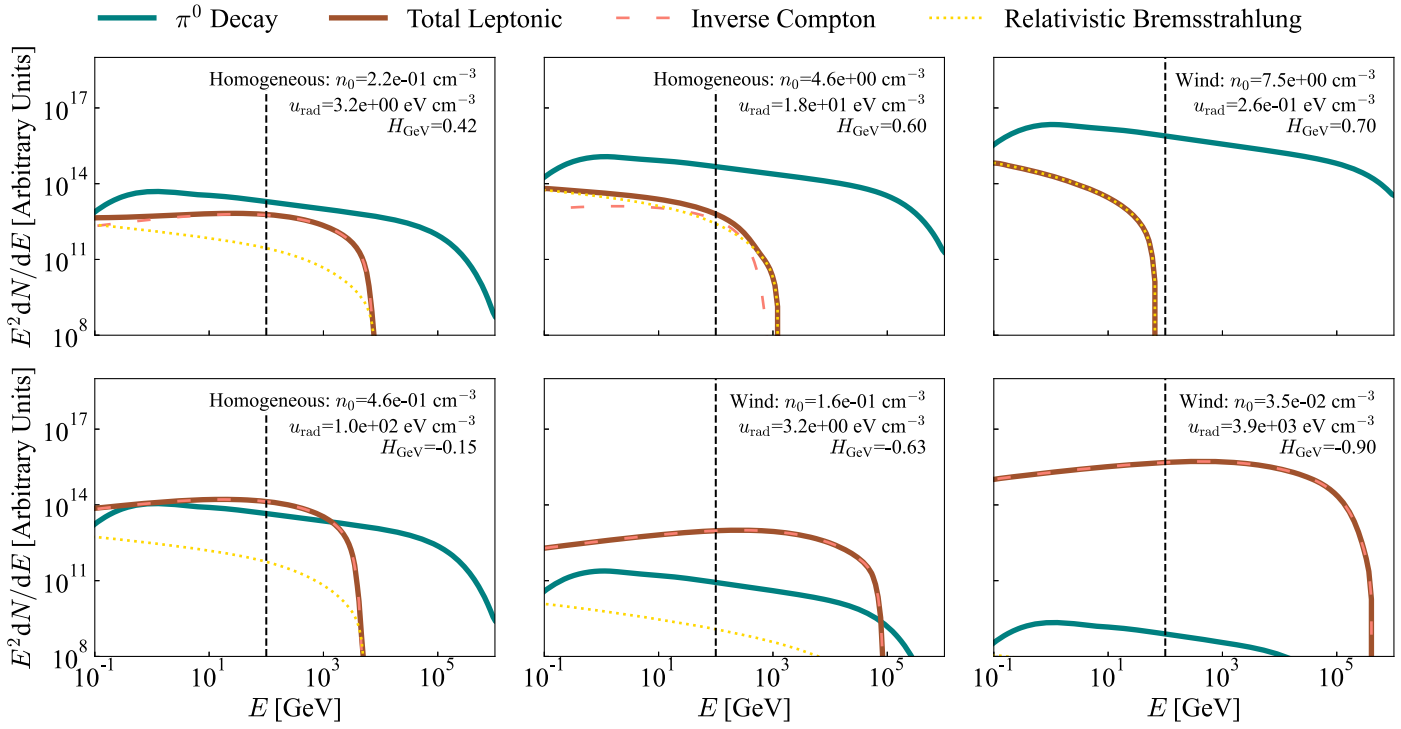

Figure 2. Cumulative hadronic γ-ray spectra (blue lines) and leptonic γ-ray spectra (red lines) at the transition between the ejecta-dominated and Sedov–Taylor stages of a modeled SNR in a sample of environments. Each panel represents a different ambient medium, with n_0 denoting the matter density normalization and u_{rad} denoting the radiation energy density. As in Figure 1, we consider both homogeneous and wind profiles for the ambient density. Vertical-black dashed lines mark 100 GeV, the dividing energy between our GeV and TeV bands. The top (bottom) panels represent hadronic (leptonic) cases with the extremity of the scenario (i.e., the absolute value of the hadronicity, H) increasing from left-hand to right-hand. Note that the nature of the underlying particle acceleration remains the same across panels. The strong variation in γ-ray emission shown here arises solely from environmental factors.

range of hadronicity. These spectra are calculated at the beginning of the Sedov stage. Across the parameter space, variation in hadronicity is exacerbated by the fact that an increase in the hadronic γ-ray luminosity typically accompanies a decrease in the leptonic luminosity, and vice-versa. Namely, the luminosity due to π_0-decay scales the ambient density, while IC emission tends to be inhibited in denser environments, where electrons tend to suffer strong synchrotron losses. Note also that relativistic bremsstrahlung is nearly always subdominant with respect to IC, except in cases of extreme hadronicity.

Figure 3, instead, depicts the time evolution of the GeV and TeV luminosities for a homogeneous profile and a wind profile. In particular, for the homogeneous scenario, in the late-Sedov stage the leptonic luminosity tends to grow faster than the hadronic luminosity, which is a consequence of the shifting of the electron cutoff to higher energies when the amplified magnetic field decreases and synchrotron losses become less severe. As a

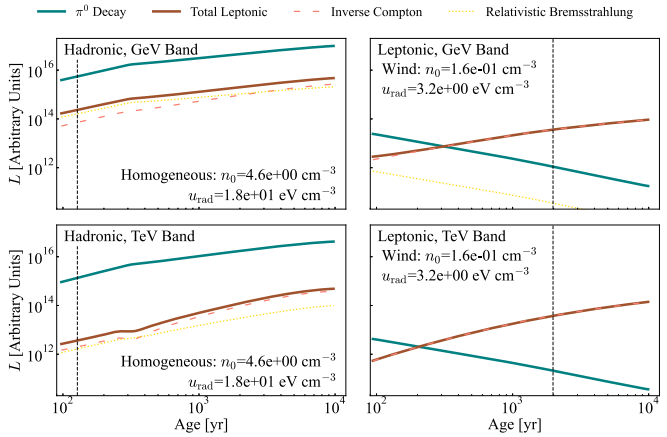

Figure 3. Time evolution of hadronic and leptonic luminosities for a moderately hadronic homogeneous profile scenario (left-hand) and a moderately leptonic wind profile scenario (right-hand). The environmental parameters are the same as those used in the middle column of Figure 2. The top (bottom) row corresponds to luminosities calculated in the GeV (TeV) band. The vertical-black dashed lines denote the onset of the Sedov–Taylor phase.

consequence, over time, there is a general trend for the spectra to become more leptonic. In the case of a wind profile, the leptonic emission monotonically increases against a monotonically decreasing hadronic curve, which results in a definitive progression toward a leptonically dominated scenario. Note that the two resulting plots are generally representative of the behavior of the time evolution of the uniform and wind profiles across their parameter spaces. The only variation comes from the relative values of the hadronic and leptonic curves as the environmental parameters are modified.

To summarize the effect of the environment on an SNR's γ-ray emission, Figure 4 shows hadronicity as a function of ambient matter density and background radiation energy density. At number densities less than order $\sim$0.1–1 cm^{-3}, where IC scattering tends to dominate leptonic emission, hadronicity increases linearly with increasing matter density and with decreasing energy density. Once the scenario becomes moderately or extremely hadronic, π^0 decay and relativistic bremsstrahlung become more dominant processes, such that the energy density dependence weakens and the hadronicity increases more purely with number density. It is also worth noting that hadronicities—both hadronic and leptonic—tend to be more extreme in the TeV band, largely due to the fact that TeV energies often sample the IC cutoff.

We summarize the effect of SNR evolution on hadronicity in Figure 5, which shows hadronicity as a function of SNR age. As stated previously, SNRs generally become more leptonic with time. Here we can see that this effect is more pronounced in wind profiles, where the ambient density decreases with radius. Homogeneous profiles also exhibit a modest decrease in hadronicity with time in the TeV band, due to the increasing IC cutoff energy. However, in this case we never find situations in which a source transitions from being dominantly hadronic to leptonic.

4. Discussion

Our analysis demonstrates that the apparent hadronicity of an SNR depends strongly on its age and the environment into which it expands. Notably, the best SNR candidates for strong hadronic emission are young and expanding into environments with high matter densities and/or low radiation energy densities. This conclusion derives from the fact that emission from π^0 decay scales with matter density, while IC emission scales with radiation energy density. Many of the candidates for hadronic SNRs identified in Caprioli (2011) and Acero et al. (2015) are indeed young and/or associated with molecular clouds. Likewise, Funk (2015) collected the spectra of several bright γ-ray sources, and those that are identified as likely hadronic are either young or exist in high density environments.

When considering GeV and TeV-band spectra, one notable pattern, as mentioned earlier, is that the TeV emission tends to exhibit more extreme hadronicity, meaning that dominantly hadronic cases become even more hadronic. This behavior may run counter to expectations because at TeV energies the hadronic spectrum is steeper than the leptonic one. However, when measuring hadronicity over a fixed energy band, the dominance of one process over another depends in large part on the position of the high-energy cutoff. In the case of IC emission, this depends on the electron cutoff, which is mediated by synchrotron losses.

Note that the γ-ray cutoff of a leptonic-dominated SNR is not representative of the maximum energy of the accelerated hadrons, which raises the question of whether γ-ray emission at energies $\gtrsim$10 TeV can be used to identify SNR PeVatrons, (i.e., as in, e.g., Cao et al. 2021; Acero et al. 2023; MAGIC Collaboration et al. 2023). Yet, since PeVatrons must have very large magnetic fields, our model suggests that their TeV emission should generally be hadronic, and thus a good probe of their ability to accelerate Galactic CRs up to the knee.

4.1. Dependence on K_{ep}

Here, we examine the effect of changing the normalization of the electron spectrum relative to the ions spectrum, $K_{\rm ep}$. Figure 6 shows the hadronicity of a SNR embedded in environments of varying density as a function of $K_{\rm ep}$. Increasing $K_{\rm ep}$ makes the SNR look more leptonic, with a scaling that can be calculated directly via Equation (3) with respect to the cases considered here.

However, a simple rescaling would not work if $K_{\rm ep}$ exhibited a strong dependence on the SNR evolution (see Figure 5) and/or environment. For instance, particle-in-cell (PIC) simulations (e.g., Amano & Hoshino 2010; Riquelme & Spitkovsky 2011; Shalaby et al. 2022) hint that electron acceleration may be enhanced when the shock Alfvénic Mach number drops below $\sqrt{m_i/m_e}/2 \sim 21$. However, that being said, this should only affect the emission of SNRs in the late-Sedov/radiative stage, especially if the dynamical role of CRs were taken into account (Diesing & Caprioli 2018). Mainly because PIC simulations of non-relativistic shocks are computationally very challenging, it has only been possible to calculate $K_{\rm ep}$ self-consistently in a few cases (e.g., Park et al. 2015; Xu et al. 2020; Shalaby et al. 2022). A theory of how $K_{\rm ep}$ depends on the shock parameters is currently missing.

The best characterization of the acceptable values of $K_{\rm ep}$ are therefore phenomenological. The analysis of individual SNRs (e.g., Berezhko & Völk 2004; Völk et al. 2005; Vladimirov et al. 2006; Morlino & Caprioli 2012; Slane et al. 2014) and of the radio emission from a complete sample of SNRs in nearby galaxies (Sarbadhicary et al. 2017) suggests values of $K_{\rm ep} \sim 10^{-4}$ to 10^{-2}. These values are consistent with those extrapolated from PIC simulations (Park et al. 2015; Xu et al. 2020; Shalaby et al. 2022) and are emphasized in Figure 6.

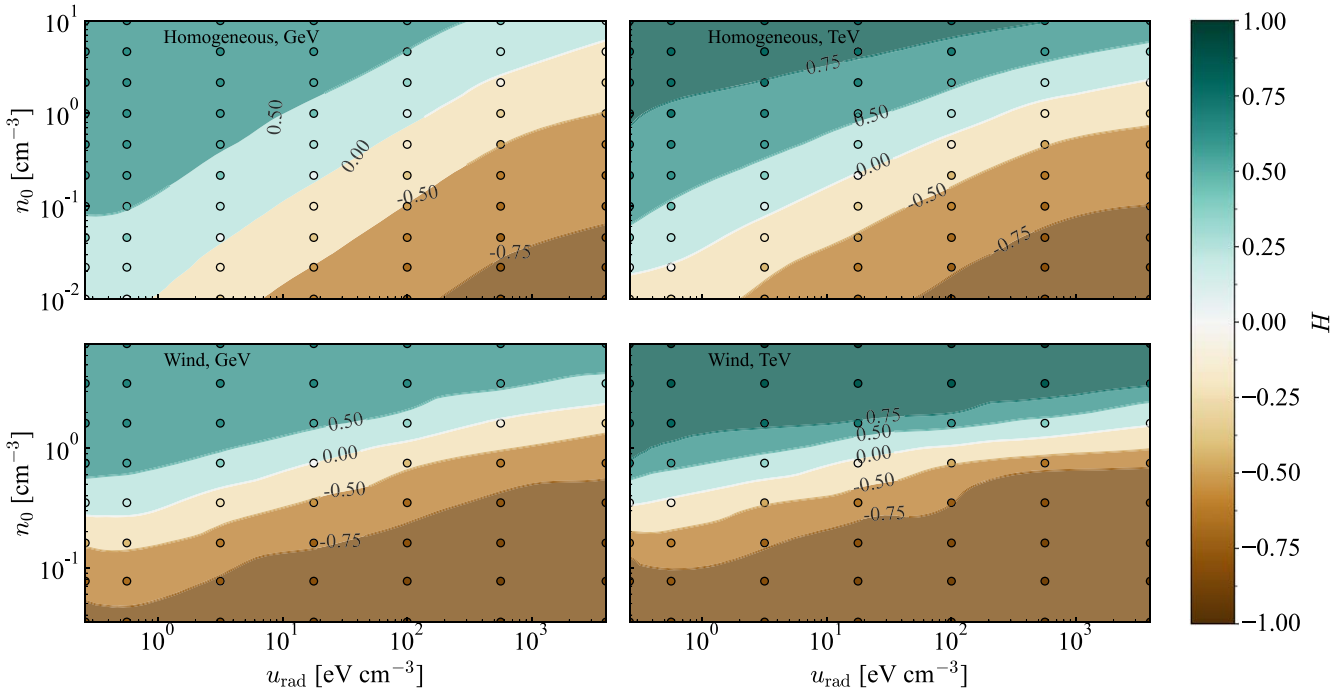

Figure 4. Hadronicity as a function of matter (n_0) and background radiation energy density ($u_{\rm rad}$). The model results are presented as data points, while the contours in the background are generated by 2D interpolation. The left-hand (right-hand) columns correspond to the GeV (TeV) bands, while the top (bottom) rows correspond to homogeneous (wind) density profiles. Broadly speaking, hadronic emission dominates in environments with high ambient density and low radiation energy density.

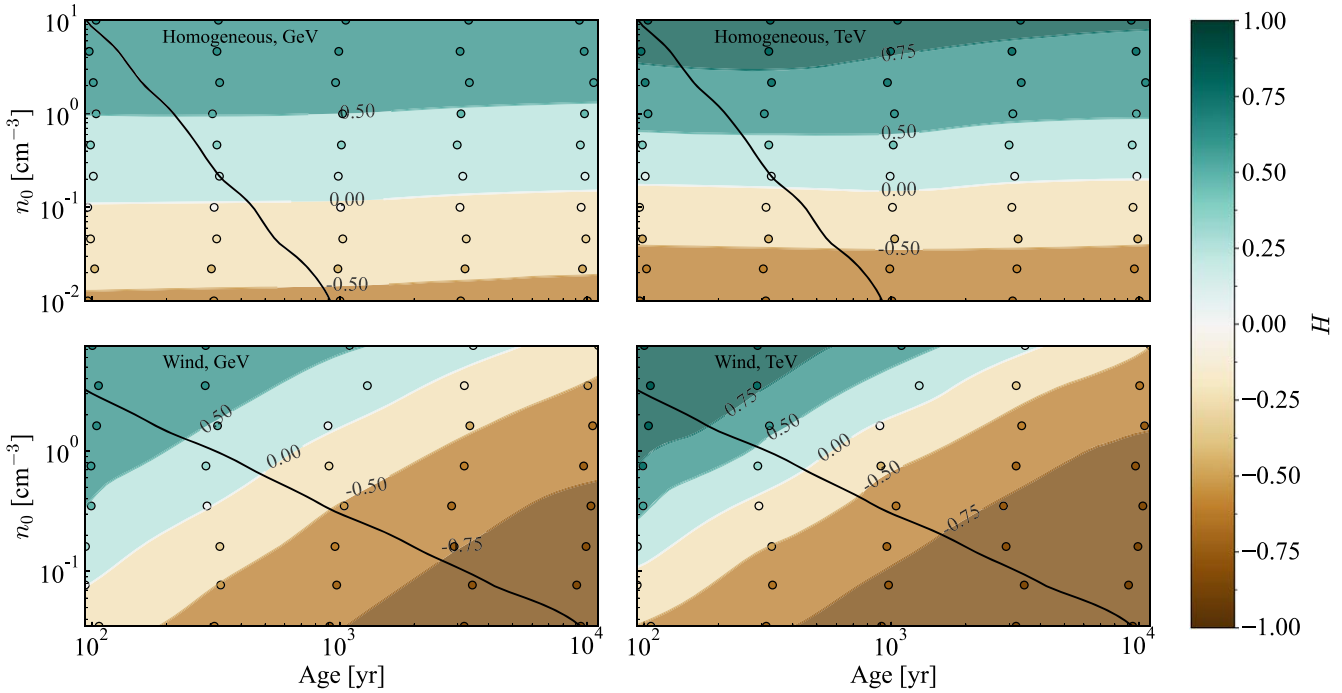

Figure 5. Hadronicity as a function of SNR age and ambient density (n_0). The model results are presented as data points, while the contours in the background are generated by 2D interpolation. The left-hand (right-hand) columns correspond to the GeV (TeV) bands, while the top (bottom) rows correspond to homogeneous (wind) density profiles. The black lines represent the Sedov–Taylor times for each density profile. In general, young SNRs tend to be the most hadronic. In all cases, the radiation field (CMB and moderate stellar background) has energy density $u_{\rm rad} = 10.3$ eV cm^{-3}.

4.2. Dependence on the Environment

We can summarize the role of the SNR environment on its γ-ray emission in terms of a simple scaling relation for hadronicity, assuming that IC dominates the leptonic emission. Assuming power-law particle spectra of the form $dN_{\rm p}/dE = K_{\rm p}E^{-q}$ and $dN_{\rm e}/dE = K_{\rm e}E^{-q}$, we construct expressions for the emissivities of the two radiative processes motivated by the derivations in Longair (2011) and Ghisellini (2013): $\epsilon_{\gamma_{\pi^0}}(E) \propto nK_{\rm p}E^{-q}$, $\epsilon_{\gamma_{\rm IC}}(E) \propto u_{\rm rad}K_{\rm e}E^{-(q-1)/2}$. These scalings are only valid at energies below the high-energy cutoff for each species. We expect these approximations to break down in the

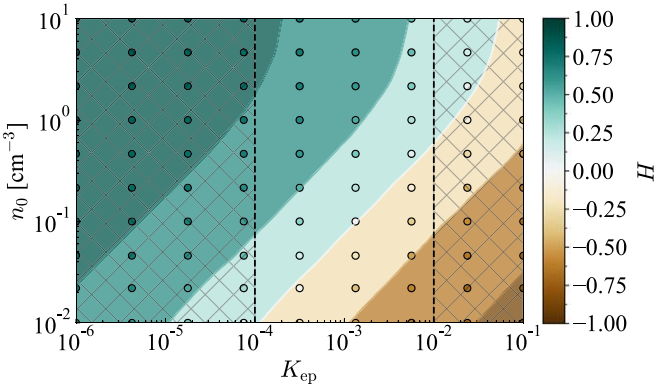

Figure 6. GeV hadronicity as a function of the relative normalization of the electron spectrum, $K_{\rm ep}$, and ambient density for homogeneous profiles. The total radiation field is fixed as $u_{\rm rad} = 10.3$ eV cm^{-3}, as was done in Figure 5. Exterior regions with hatch marks bound the region $K_{\rm ep} \sim 10^{-4}$ to 10^{-2}, which broadly reflects the observed range of values.

TeV band when electron synchrotron losses are important (Diesing & Caprioli 2019). Posing $K_{\rm ep} = K_{\rm e}/K_{\rm p}$, the ratio of these two expressions scales as,

$$\frac{\epsilon_{\gamma_{\pi^0}}}{\epsilon_{\gamma_{\rm IC}}} \propto \frac{n}{K_{\rm ep} u_{\rm rad} E^{(q+1)/2}}, \tag{4}$$

Using the results of our hadronicity calculations in a homogeneous medium to estimate the normalization of this expression, we obtain,

$$\frac{\epsilon_{\gamma_{\pi^0}}}{\epsilon_{\gamma_{\rm IC}}} \simeq 44 \left(\frac{10^{-3}}{K_{\rm ep}}\right)\left(\frac{n}{\rm cm^{-3}}\right)\left(\frac{\rm eV\ cm^{-3}}{u_{\rm rad}}\right)\left(\frac{\rm GeV}{E}\right)^{\frac{q+1}{2}}. \tag{5}$$

This formula is in good agreement with the top left-hand panel of Figure 4. The story is somewhat more complicated for expansion in a wind profile, for which this simple single-zone model is not necessarily a good approximation. In addition, this may underestimate the hadronicity in the TeV band, where radiative losses may suppress the electron spectrum. Eventually, we argue that in the absence of detailed information about a SNR expansion history, this expression still holds as a rough estimate of the hadronicity.

Generally speaking, the trends that we have identified are consistent across both homogeneous and wind profiles. The most notable difference is that in a decreasing density profile, SNRs may exhibit more leptonic emissions as they age. Physically speaking, any wind profile should terminate at some finite distance (Weaver et al. 1977; Ptuskin & Zirakashvili 2005), beyond which the emission should be similar to that of a SNR expanding in the homogeneous ISM (Caprioli 2011). Furthermore, beyond a power-law scaling with radius, none of our profiles include inhomogeneities (i.e., clumps, molecular clouds, or ISM-scale gradients), which would certainly be present in realistic scenarios. Since the matter density of clouds would be greater than their ambient surroundings, our results suggest that that they would increase the hadronicity of an observed source. Therefore, Equation (5) also likely represents a lower limit on the actual hadronicity in this case.

5. Conclusion

In summary, we modeled time-dependent and multi-zone CR acceleration in an evolving SNR using a semi-analytical implementation of non-linear DSA. Our goal was to understand the factors that influence whether a SNR emission is dominated by hadronic or leptonic processes. For a fixed supernova explosion, the dominance of hadronic or leptonic emission is likely to be governed by environmental factors, rather than by the underlying nature of particle acceleration, in the sense that —for typical ISM parameters— the same accelerator would look more/less hadronic depending on its environment.

Furthermore, we find that SNRs may appear more leptonic as they age—particularly in the TeV band—due to decreases in the amplified magnetic field, and thus increases in the synchrotron-limited maximum electron energy. This transition is even more pronounced in SNRs expanding into media with decreasing density, such as pre-SN stellar winds. This is true before the shock hits the ISM "wall" (Weaver et al. 1977) and in the absence of local density enhancements, such as molecular regions, which would naturally boost the hadronic signal. Thus, our findings suggest that the best candidates bearing signatures of hadron acceleration are young core-collapse SNRs, as well as SNRs interacting with molecular clouds.

More quantitatively, SNRs expanding into media with $[n/({\rm cm^{-3}})]/[u_{\rm rad}/({\rm eV\ cm^{-3}})] \gtrsim 2$ are likely to exhibit hadronic signatures, even in the case of very efficient electron acceleration ($K_{\rm ep} \lesssim 10^{-2}$). These findings may guide the interpretation of data from very-high-energy γ-ray observatories such as HESS, MAGIC, VERITAS, LHAASO, and, in the near future, CTA. To inform these observations, we have introduced the hadronicity parameter, H, which can help direct them toward sources that are more likely to be hadronic. It should be noted, however, that observations of a source in both the GeV and TeV bands provide the most compelling case for whether the source is hadronic or leptonic: since particle spectra are expected to be $\propto E^{-2}$ or steeper, any GeV-to-TeV spectrum steeper than E^{-2} is a strong indication of hadronic emission (e.g., Caprioli 2011).

Finally, we propose that the hadronicity H (Equation (3)) and the scaling in Equation (5) can be used as indicators of the probability that a SNR may be a source of high-energy neutrinos in the TeV band. The sensitivity of current neutrino telescopes (i.e., Ice Cube and Antares) is not likely to be high enough to detect individual SNR sources, but may be sufficient to conduct a stacked analysis of candidate sources, and hadronicity may represent an effective sorting parameter. The next generation of very-high-energy neutrino observatories (e.g., KM3NET, IceCube–Gen2, TRIDENT, and P-One) have the potential to fully unravel the nature of SNRs as hadron accelerators and, in turn, as the sources of Galactic CRs.

Acknowledgments

We thank the anonymous referee for their comments, which helped to improve the clarity of this paper. This research was partially supported by NASA grant 80NSSC20K1273 and the NSF grants AST-1909778, AST-2009326, and PHY-2010240.

ORCID iDs

Nicholas J. Corso https://orcid.org/0000-0002-0088-2563
Rebecca Diesing https://orcid.org/0000-0002-6679-0012
Damiano Caprioli https://orcid.org/0000-0003-0939-8775

References

Abdo, A. A., Ackermann, M., Ajello, M., et al. 2011, ApJ, 734, 28
Acciari, V. A., Ansoldi, S., Antonelli, L. A., et al. 2022, NatAs, 6, 689
Acero, F., Acharyya, A., Adam, R., et al. 2023, APh, 150, 102850
Acero, F., Ackermann, M., Ajello, M., et al. 2015, ApJS, 218, 23
Ackermann, M., Ajello, M., Allafort, A., et al. 2013, Sci, 339, 807
Aharonian, F., Akhperjanian, A. G., Bazer-Bachi, A. R., et al. 2006, A&A, 449, 223
Aharonian, F., Benkhali, F. A., Angüner, E. O., et al. 2022, Sci, 376, 77
Aharonian, F. A., Kelner, S. R., & Prosekin, A. Y. 2010, PhRvD, 82, 043002
Amano, T., & Hoshino, M. 2010, PhRvL, 104, 181102
Amato, E., & Blasi, P. 2005, MNRAS, 364, L76
Amato, E., & Blasi, P. 2006, MNRAS, 371, 1251
Amato, E., & Blasi, P. 2009, MNRAS, 392, 1591
Bandiera, R., & Petruk, O. 2010, A&A, 509, A34
Baring, M. G., Ellison, D. C., Reynolds, S. P., Grenier, I. A., & Goret, P. 1999, ApJ, 513, 311
Bell, A. R. 2004, MNRAS, 353, 550
Berezhko, E. G., Ksenofontov, L. T., & Völk, H. J. 2006, A&A, 452, 217
Berezhko, E. G., & Völk, H. J. 2004, A&A, 427, 525
Berezhko, E. G., & Völk, H. J. 2006, A&A, 451, 981
Berezhko, E. G., & Völk, H. J. 2007, ApJL, 661, L175
Bisnovatyi-Kogan, G. S., & Silich, S. A. 1995, RvMP, 67, 661
Blasi, P. 2002, APh, 16, 429
Blasi, P. 2004, APh, 21, 45
Blasi, P. 2010, MNRAS, 402, 2807
Blasi, P. 2019, NCimR, 42, 549
Blasi, P., Amato, E., & Caprioli, D. 2007, MNRAS, 375, 1471
Blasi, P., Morlino, G., Bandiera, R., Amato, E., & Caprioli, D. 2012, ApJ, 755, 121
Cao, Z., Aharonian, F. A., An, Q., et al. 2021, Natur, 594, 33
Caprioli, D. 2011, JCAP, 2011, 26
Caprioli, D. 2012, JCAP, 2012, 38
Caprioli, D., Amato, E., & Blasi, P. 2010a, APh, 33, 160
Caprioli, D., Amato, E., & Blasi, P. 2010b, APh, 33, 307
Caprioli, D., Blasi, P., Amato, E., & Vietri, M. 2009, MNRAS, 395, 895
Caprioli, D., Haggerty, C. C., & Blasi, P. 2020, ApJ, 905, 2
Caprioli, D., Pop, A., & Spitkovsky, A. 2015, ApJL, 798, 28
Caprioli, D., & Spitkovsky, A. 2014a, ApJ, 783, 91
Caprioli, D., & Spitkovsky, A. 2014b, ApJ, 794, 46
Caprioli, D., & Spitkovsky, A. 2014c, ApJ, 794, 47
Caprioli, D., Yi, D. T., & Spitkovsky, A. 2017, PhRvL, 119, 171101
Caprioli, D., Zhang, H., & Spitkovsky, A. 2018, JPlPh, 84, 715840301
Case, G. L., & Bhattacharya, D. 1998, ApJ, 504, 761
Chevalier, R. A. 1998, ApJ, 499, 810
Cristofari, P., Blasi, P., & Caprioli, D. 2021, A&A, 650, A62
Diesing, R. 2023, arXiv:2305.07697
Diesing, R., & Caprioli, D. 2018, PhRvL, 121, 091101
Diesing, R., & Caprioli, D. 2019, PhRvL, 123, 071101
Diesing, R., & Caprioli, D. 2021, ApJ, 922, 1
Diesing, R., Metzger, B. D., Aydi, E., et al. 2023, ApJ, 947, 70
Draine, B. T. 2011, Physics of the Interstellar and Intergalactic Medium (Princeton, NJ: Princeton Univ. Press), 119
Ellison, D. C., Patnaude, D. J., Slane, P., Blasi, P., & Gabici, S. 2007, ApJ, 661, 879
Ellison, D. C., Patnaude, D. J., Slane, P., & Raymond, J. 2010, ApJ, 712, 287
Funk, S. 2015, ARNPS, 65, 245
Ghisellini, G. 2013, Radiative Processes in High Energy Astrophysics, 873 (Cham: Springer), 79
Giuffrida, R., Miceli, M., Caprioli, D., et al. 2022, NatCo, 13, 5098
Guo, X., Sironi, L., & Narayan, R. 2014, ApJ, 794, 153
Haggerty, C. C., & Caprioli, D. 2020, ApJ, 905, 1
Hillas, A. M. 2005, JPhG, 31, 95
Kafexhiu, E., Aharonian, F., Taylor, A. M., & Vila, G. S. 2014, PhRvD, 90, 123014
Khangulyan, D., Aharonian, F. A., & Kelner, S. R. 2014, ApJ, 783, 100
Lagage, P. O., & Cesarsky, C. J. 1983, A&A, 118, 223
Lee, S.-H., Slane, P. O., Ellison, D. C., Nagataki, S., & Patnaude, D. J. 2013, ApJ, 767, 20
Longair, M. S. 2011, High Energy Astrophysics (3rd ed.; Cambridge: Cambridge Univ. Press), 503
MAGIC Collaboration, Abe, H., Abe, S., et al. 2023, A&A, 671, A12
Malkov, M. A. 1997, ApJ, 485, 638
Malkov, M. A., Diamond, P. H., & Völk, H. J. 2000, ApJL, 533, L171
Morlino, G., Amato, E., & Blasi, P. 2009, MNRAS, 392, 240
Morlino, G., Blasi, P., Bandiera, R., Amato, E., & Caprioli, D. 2013, ApJ, 768, 148
Morlino, G., & Caprioli, D. 2012, A&A, 538, A81
Morlino, G., & Celli, S. 2021, MNRAS, 508, 6142
O'C. Drury, L., Aharonian, F., & Völk, H. J. 1994, A&A, 287, 959
Ostriker, J. P., & McKee, C. F. 1988, RvMP, 60, 1
Pais, M., & Pfrommer, C. 2020, MNRAS, 498, 5557
Park, J., Caprioli, D., & Spitkovsky, A. 2015, PhRvL, 114, 085003
Ptuskin, V., Zirakashvili, V., & Seo, E.-S. 2010, ApJ, 718, 31
Ptuskin, V. S., & Zirakashvili, V. N. 2005, A&A, 429, 755
Reville, B., & Bell, A. R. 2013, MNRAS, 430, 2873
Riquelme, M. A., & Spitkovsky, A. 2011, ApJ, 733, 63
Sarbadhicary, S. K., Badenes, C., Chomiuk, L., Caprioli, D., & Huizenga, D. 2017, MNRAS, 464, 2326
Shalaby, M., Lemmerz, R., Thomas, T., & Pfrommer, C. 2022, ApJ, 932, 86
Slane, P., Lee, S.-H., Ellison, D. C., et al. 2014, ApJ, 783, 33
Vladimirov, A., Ellison, D. C., & Bykov, A. 2006, ApJ, 652, 1246
Völk, H. J., Berezhko, E. G., & Ksenofontov, L. T. 2005, A&A, 433, 229
Weaver, R., McCray, R., Castor, J., Shapiro, P., & Moore, R. 1977, ApJ, 218, 377
Winner, G., Pfrommer, C., Girichidis, P., Werhahn, M., & Pais, M. 2020, MNRAS, 499, 2785
Xu, R., Spitkovsky, A., & Caprioli, D. 2020, ApJL, 897, L41
Yuan, Q., Liu, S., & Bi, X. 2012, ApJ, 761, 133
Zabalza, V. 2015, ICRC (The Hague), 34, 922
Zirakashvili, V. N., & Aharonian, F. 2007, A&A, 465, 695
Zirakashvili, V. N., & Aharonian, F. A. 2010, ApJ, 708, 965